

# Model-Based Uncertainty Quantification for the Product Properties of Lithium-Ion Batteries

Vincent Laue, Oke Schmidt, Henning Dreger, Xiangzhong Xie, Fridolin Röder, René Schenkendorf, Arno Kwade, and Ulrike Krewer\*

A model-based uncertainty quantification (UQ) approach is applied to the manufacturing process of lithium-ion batteries (LIB). Cell-to-cell deviations and the influence of sub-cell level variations in the material and electrode properties of the cell performance are investigated experimentally and via modeling. The electrochemical battery model of the Doyle–Newman type is extended to cover the effect of sub-cell deviation of product properties of the LIB. The applied model is parameterized and validated using a stacked pouch cell containing  $\text{Li}(\text{Ni}_{1/3}\text{Co}_{1/3}\text{Mn}_{1/3})\text{O}_2$  (NMC) and graphite ( $\text{Li}_x\text{C}_6$ ). It is integrated into a sampling-based UQ framework. A nested point estimate method (PEM) is applied to a large number of independent normal distributed parameters. The simulations follow two consecutive nonideal manufacturing process steps: coating and calendering. The nested PEM provides a global sensitivity analysis that shows a change in sensitivity of the investigated parameters depending on the applied C-rate. Furthermore, the sub-cell level deviation of parameters in heterogeneous electrodes provokes a nonuniform current distribution in the cell. This alters the variance of the discharge capacity distribution. Therefore, sub-cell deviation has to be considered to quantify process uncertainties. The applied method is feasible and highly efficient for this purpose.

## 1. Introduction


The manufacturing process of lithium-ion batteries (LIBs) contains many process parameters. Their influence on the product performance is often nonlinear and not well understood, especially in quantitative terms. However, to achieve a product that exhibits good performance and meets quality goals such as high energy density and low costs, the manufacturing process has to be optimized and uncertainties of process and product parameters have to be dealt with.<sup>[1]</sup> Knowledge about process uncertainties and their influence on the product performance can enable a robust optimization of cell design and balancing. Two processes have a significant impact on the product: first, the coating process of the slurry of active material, carbon black (CB), and binder on the metallic

substrate, and second, the subsequent compression of the coated particle layer, called calendering. Both processes have a significant influence on the electrode properties, such as electrolyte phase volume fraction, electrode thickness, and effective conductivity. The influence of calendering is investigated experimentally in refs. [2–7] and by simulation in refs. [2,3,8]. In addition, thermodynamic properties of the active material will deviate due to processes before the actual manufacturing process; for example, the specific capacity of graphite is dependent on the degree of disorder, which is caused by the temperature in the prior processes.<sup>[9]</sup>

Due to the crucial need for an advanced process, the application of uncertainty quantification (UQ) methods to the manufacturing process of LIBs has gained interest.<sup>[10–13]</sup> In addition to the common modeling approaches as reviewed in ref. [14], UQ provides quantitative information about the interaction between different parameters and enables the adaption of production quality measures to the specific produced battery. As a model-based approach, UQ can partially substitute the frequently used time- and cost-intensive experimental approaches.

In the context of LIBs, there are different approaches of UQ or uncertainty propagation (UP). They are classified into sample-based, or direct, methods and indirect methods that adapt the system. The sample-based methods include, for example, Monte Carlo (MC) simulations wherein the system is evaluated with random parameter sets. For instance, Kenney et al. quantified the influence of process variations related to layer thickness, electrode density, and the amount of active material by evaluating a serial set of single particle models (SPMs) with randomly chosen parameter sets in each model.<sup>[12]</sup> Indirect methods include polynomial chaos expansion (PCE), see ref. [15], wherein variations in the particle size were addressed, and methods of control

V. Laue, O. Schmidt, X. Xie, F. Röder, Dr. R. Schenkendorf, Prof. U. Krewer  
Institute of Energy and Process Systems Engineering  
TU Braunschweig  
Franz-Liszt-Strasse 35, D-38106 Braunschweig, Germany  
E-mail: u.krewer@tu-braunschweig.de

 The ORCID identification number(s) for the author(s) of this article can be found under <https://doi.org/10.1002/ente.201900201>.

DOI: 10.1002/ente.201900201

V. Laue, O. Schmidt, H. Dreger, F. Röder, Prof. A. Kwade, Prof. U. Krewer  
Battery LabFactory Braunschweig (BLB)  
TU Braunschweig  
D-38106 Braunschweig, Germany

H. Dreger, Prof. A. Kwade  
Institute for Particle Technology  
TU Braunschweig  
Volkmaroder Strasse 5, D-38104 Braunschweig, Germany

theory as used in ref. [16], wherein an analytic model of the battery's impedance response was applied, considering variations in porosity, particle size, and layer thickness. The former is limited to a low number of uncertain parameters and the latter provides only upper and lower bounds of the uncertain output.<sup>[15]</sup>

In addition to the usage of UQ to investigate the UP between product parameters and cell performance, UQ also can provide a sensitivity analysis (SA) for parameter estimation and parameterization of physics-based models.<sup>[17,18]</sup> Especially for parameterization, the number of uncertain parameters is large compared with UP investigations. For instance, Schmidt et al. considered 33 uncertain parameters in a single model. They applied SA based on the Fisher information matrix.<sup>[19]</sup> More recently, Lin et al. applied PCE to a 3D multiphysics battery model to conduct a global SA.<sup>[20]</sup>

In the literature, different distribution shapes and widths are observed. For example, Schuster et al. and Dubarry et al. showed deviations of quantities such as weight, capacity, and resistance variations from  $\pm 0.1\%$  to  $\pm 5.7\%$  considering partially normal and partially Weibull distributions,<sup>[21,22]</sup> whereas Vazquez-Arenas et al. assumed a normal distribution with variations of  $\pm 10\%$ ,<sup>[17]</sup> and Kenney et al. investigated electrodes assuming variances between 1% and 5%.<sup>[12]</sup> Recently, Röder et al. investigated the impact of particle size distribution and its shape considering Weibull distribution.<sup>[23]</sup>

As mentioned above, common uncertain parameters are layer thickness, porosity, and particle size. It is noteworthy that there are significant differences in distributions of macroscopic quantities such as layer thickness and microscopic quantities such as particle size. In general, four different kinds of parameter distributions have to be considered. The scale of these parameter deviations is illustrated in **Figure 1**. First, parameters may be distributed on particle level due to the processing before the electrode and cell production, for example, particle size.<sup>[23–25]</sup> In addition, its distribution corresponds to the used active material. Second, there are local changes in macroscopic quantities such as porosity due to small-scale process deviations. These deviations occur at the scale of a single electrode sheet or below, termed sub-cell, and they are influenced by process steps such as mixing,<sup>[26–28]</sup> calendaring,<sup>[2–7,28]</sup> and drying.<sup>[29]</sup> Third, there are cell-to-cell deviations of macroscopic quantities such as layer thickness.<sup>[11–13,21,22]</sup> These deviations are caused by process deviations, which occur at large scales compared with the size of the electrode of a whole cell. Fourth, there are lot-to-lot or batch deviations occurring between lots or batches produced, for example, on different days.<sup>[16,21]</sup> However, these deviations are neglected in this work. To the best of the author's knowledge, the combined effect of the first three kinds of deviations have only been the subject of simulation studies implicitly, in so far as real 3D structures were considered, but not as an effect of the production process. These models are computationally time-consuming and prone to numerical issues. In addition, the effects of single parameter distributions are indistinct, and thus, an unambiguous assignment is not possible.

In this article, a mathematical model is introduced that is feasible to simulate process deviations on a sub-cell level (second kind). Parameter distributions of the first kind could easily be included in the model, but they are beyond the scope of this article, which focuses on a novel approach to the model distributions of electrode properties on a sub-cell level. The introduced

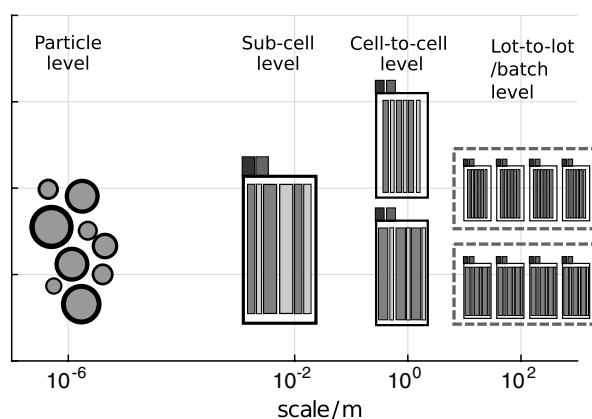


**Figure 1.** Scale of deviations from particle to lot level.

model's computational cost is significantly lower than those of the real 3D models. For classification of models and their computational cost, it is referred to the review of Ramadesigan et al.<sup>[30]</sup> As the proposed model considers sub-cell level deviations, it is of special interest for stacked pouch cells as described in Section 3.

By applying this model to an exemplary LIB, global SA and UQ are presented.

## 2. Mathematical Model

In this section, the methodology applied in this work is introduced. A given LIB, containing state-of-the-art active material, is simulated by a physics-based model, and the model is evaluated using a sample-based UQ approach.

### 2.1. Uncertainty Quantification Using Monte Carlo Simulations

Monte Carlo (MC) simulations are commonly used for UQ. MC simulations generate samples from the probability distribution via random inputs using different sample techniques and estimate the statistical information of the model output. Consider a model  $F(X_1, X_2, \dots, X_N) \in \mathbb{R}^N$ . From the parameter space for  $(X_1, X_2, \dots, X_N)$ , a finite number  $m$  of sample points  $\xi_i = (X_{1,i}, X_{2,i}, \dots, X_{N,i}), \forall i \in \{1, \dots, m\}$  are drawn randomly. The model is then evaluated, leading to  $m$  simulated observations of the model output:  $Z_i = F(\xi_i), \forall i \in \{1, \dots, m\}$ , which can be evaluated in terms of mean value and variance if a sufficient number of samples are drawn. The method is straightforward for implementation and can provide accurate estimation. In the context of batteries, MC was applied, for example, by Mendoza et al.<sup>[31]</sup> and López et al.<sup>[32]</sup> However, the computational cost is often, as in this case, unaffordable because it requires a large number of model evaluations to approximate the real statistical information of the model output. Alternatively, the point estimate method (PEM) can be used, as it requires fewer model evaluations compared with MC simulations.

In this work, MC simulations are used for cases where PEM could lead to misleading results and for comparison and validation of PEM. Therefore, random sample points of deviating electrode properties are generated and C-rate tests are simulated. The

large number of sample points enables the discussion of mean value and shape of probability density function (PDF) of the model output. This approach was applied in ref. [12].

### 2.2. Applied Uncertainty Quantification Approach

PEM was introduced by Tyler<sup>[33]</sup> in 1953 and Rosenblueth<sup>[34]</sup> in 1975 and is frequently used, for example, by Lin and Li,<sup>[35]</sup> to reconstruct the PDF of an output variable  $Z$  of a nonlinear function

$$Z = F(X_1, X_2, \dots, X_N) \in \mathbb{R}^N \quad (1)$$

based on a finite number of sampling points of the  $N$  uncertain variables  $(X_1, X_2, \dots, X_N)$ . As illustrated in **Figure 2**, different uncertain input variables with different distribution widths can be considered. While  $F$  can be a black box, differentiability

of  $F$  is beneficial because a nondifferential function could cause physically meaningless results.<sup>[35]</sup>

Next, a UQ framework is used, introduced as PEM5 in ref. [36] and references therein. This method requires  $2N^2 + 1$  sampling points, which is significantly less than the number of sample points an MC approach would require normally. For instance, assuming three uncertain parameters  $(X_1, X_2, X_3)$ , which are normally distributed with  $\bar{X}_i = 0, \forall i \in \{1, \dots, 3\}$ , there are 19 sample points  $(\xi_i, \forall i \in \{1, \dots, 19\})$ . The three generator functions  $GF[\cdot]$  of the sample points are as follows

$$GF[0] = \{(0, 0, 0)^T\}, \quad (2)$$

$$GF[\pm v] = \{(v, 0, 0)^T, (-v, 0, 0)^T, (0, v, 0)^T, (0, -v, 0)^T, (0, 0, v)^T, (0, 0, -v)^T\} \quad (3)$$

and

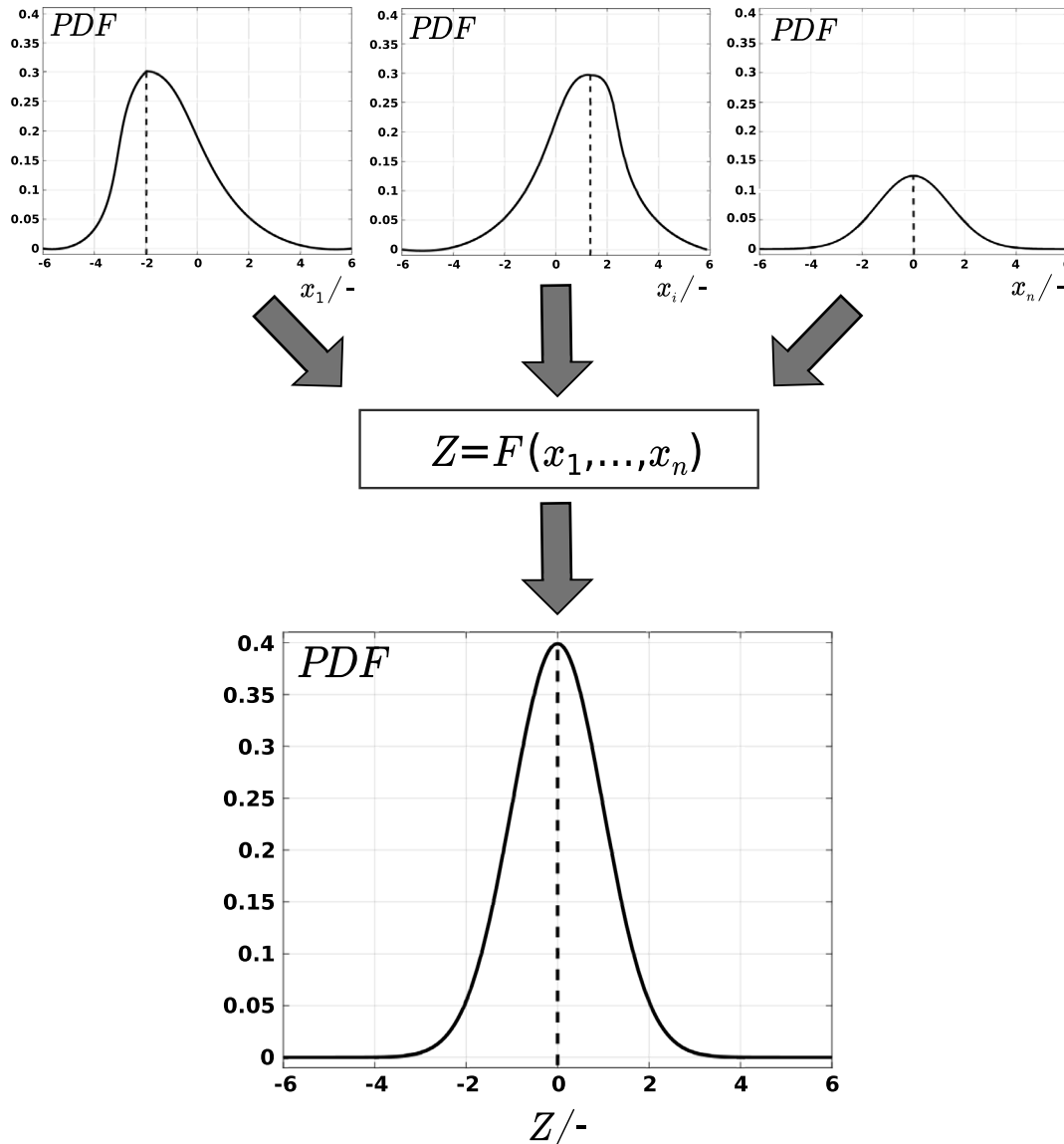


**Figure 2.** Flow chart of uncertainties for a generic function  $Z = F(X_1, X_2, X_3) \in \mathbb{R}^3$ .

$$GF[\pm v, \pm v] = \{(v, v, 0)^T, (-v, -v, 0)^T, (v, -v, 0)^T, (-v, v, 0)^T, (v, 0, v)^T, (-v, 0, -v)^T, (v, 0, -v)^T, (-v, 0, v)^T, (0, v, v)^T, (0, -v, -v)^T, (0, v, -v)^T, (0, -v, v)^T\}, \quad (4)$$

where  $v$  is a scalar parameter.

In general, the first sample point,  $\xi_1$ , would be  $(\bar{X}_1, \bar{X}_2, \bar{X}_3)^T$  and the second sample point,  $\xi_2$ , would be  $(\bar{X}_1 + v, \bar{X}_2, \bar{X}_3)^T$ . But as  $\bar{X}_i = 0, \forall i$ , all  $\bar{X}_i$  are spared in Equation (2)–(4). **Figure 3** illustrates the positions of these sample points for a 3D model. By introducing weights  $w_j, \forall j \in \{0, \dots, 2\}$ , this leads, for the 3D case, to the following expansion

$$\int_{\Omega} F(\xi) p d f_{\xi} d \xi \approx w_0 \times F(GF[0]) + w_1 \times \sum F(GF[\pm v]) + w_2 \times \sum F(GF[\pm v, \pm v]) \quad (5)$$

From this expansion, the mean value  $\bar{Z}$  and variance  $\sigma$  of the result  $Z$  are derived as follows

$$\bar{Z} \approx w_0 \times Z_0 + w_1 \sum_{i=1}^{2n} Z_i \quad (6a)$$

$$\sigma^2 \approx w_0(Z_0 - \bar{Z}) \cdot (Z_0 - \bar{Z})^T + w_1 \sum_{i=1}^{2n} (Z_i - \bar{Z}) \times (Z_i - \bar{Z})^T \quad (6b)$$

Furthermore, determination of the moments of  $Z$  and for a normally distributed  $Z$  of the PDF of  $Z$  would be possible. For further details, see ref. [36] and references therein. Using these variances, Sobol indices are determined for the global SA.<sup>[37]</sup> Neglecting higher order interactions, these indices can be defined as follows

$$S_i = \frac{\sigma_i}{\sigma} \quad (7a)$$

$$S_{i,j} = \frac{\sigma_{i,j}}{\sigma} \quad (7b)$$

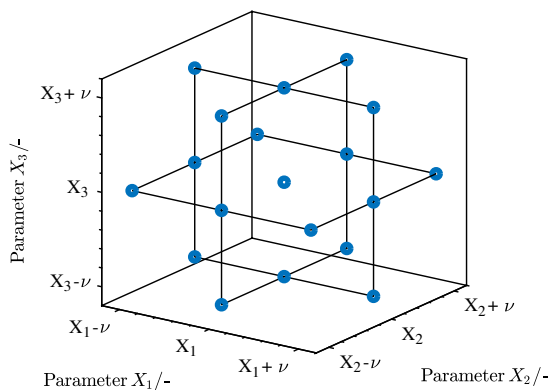


**Figure 3.** Position of the  $2N^2 + 1$  sample points  $\xi_i$  for a generic function  $Z = F(X_1, X_2, X_3) \in \mathbb{R}^3$ .

$$S_{T_i} = S_i + \sum_{j=1}^N S_{i,j} \quad (7c)$$

where  $\sigma$  is the variance of  $Z$  and  $\sigma_i$  and  $\sigma_{i,j}$  are the partial variances, respectively. In general,  $\sigma$  is a measure of the width of the distribution of the output  $Z$  of the nonlinear equation  $F$  defined in Equation (1), as it is a measure of the sensitivity of output  $Z$  to the input variables. The partial variance  $\sigma_i$ , related to the variable  $X_i$ , is a measure of sensitivity of  $Z$  to  $X_i$ . The second-order partial variance  $\sigma_{i,j}$  is a measure to which extent a change in  $X_i$  can eliminate the impact of a change in  $X_j$  on the output  $Z$ . Thus, the latter considers the interaction of the uncertain parameters  $X_i$  and  $X_j$ .<sup>[37]</sup> For a general definition of the variance and the partial variances, ref. [37] is referred (Chapter 15.1.1, pp. 323–326). Commonly, an SA is conducted for model reduction, parameter grouping, or parameter estimation purposes.<sup>[17,19,38]</sup> In this work, sensitivity is used to assess whether the deviations of product properties have a significant influence on the product performance.

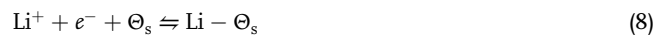
In this article, the nonlinear function  $F(\cdot)$  is a battery model as introduced in the following sections; the uncertain variables  $X_i$  are the normally distributed cell properties, and the output variable  $Z$  is the cell's discharge voltage at a specified discharge rate and time, that is, state of charge (SOC). For comparison with common experimental characteristic values, the cell voltage at 50% SOC and the discharge capacity at a voltage of 2.9 V are extracted from the discharge curves.

### 2.3. Battery Model

In this section, the two applied mathematical models are described: 1) a homogenized standard P2D model and 2) the extended model that also considers distributed electrode properties on a sub-cell level. Both are based on the pseudo-2D (P2D) electrochemical model introduced by Doyle et al. and further developed, among others, by Legrand et al.<sup>[39–41]</sup> Discretization is performed in  $x$ -direction from anode to cathode and in  $r$ -direction from the particle center to the particle surface. In addition, relevant equations and assumptions of the P2D are briefly introduced. For further details, refs. [39–41] are referred.

#### 2.3.1. Governing Equations of the P2D-Model

A dual intercalation cell is implemented, considering the following reaction at both electrodes<sup>[39]</sup>



where  $\Theta_s$  is a free space lattice in the intercalation material (solid) and  $\text{Li} - \Theta_s$  is an intercalated lithium atom. The reaction kinetics are described using a Butler–Volmer-type expression, see Equation (14) in **Table 1**. The reaction fluxes  $j^{Li}(x)$  occurring at the particle surface provide the boundary conditions for the mass transport processes in solid and electrolyte, described in Equation (9) and (11), respectively. Conservation of charge and mass is ensured by Equation (9)–(12). At the particle surfaces of both electrodes, a double layer is considered,<sup>[41]</sup> see Equation (13). This double layer is relevant for the short time

**Table 1.** Extract of the governing equations of the P2D standard model.

Equations	Boundary conditions
$\frac{\partial c_s}{\partial t} = \frac{1}{r^2} \frac{\partial}{\partial r} \left( D_s r^2 \frac{\partial c_s}{\partial r} \right) \quad (9)$	$\frac{\partial c_s}{\partial r} = \frac{-j^{Li}}{z \times F \times a_s \times D_s}, \quad r = R_p \quad (16)$
$j^{tot} = \frac{\partial}{\partial x} \left( \sigma_{s,eff} \frac{\partial \phi_s}{\partial x} \right) \quad (10)$	$\frac{\partial c_s}{\partial r} = 0, \quad r = 0 \quad (17)$
$\varepsilon \frac{\partial c_e}{\partial t} = \frac{\partial}{\partial x} \left( D_{e,eff} \frac{\partial c_e}{\partial x} \right) + (1 - t_p) \frac{j^{Li}(x)}{F} \quad (11)$	$\frac{\partial c_e}{\partial x} = 0, \quad x = \{0, L\} \quad (18)$
$j^{tot} = -\frac{\partial}{\partial x} \left( \sigma_{e,eff} \frac{\partial \phi_e}{\partial x} \right) - 2 \frac{RT}{F} (t_p - 1) \sigma_{e,eff} \frac{\partial \ln c_e}{\partial x} \quad (12)$	$\frac{\partial \phi_s}{\partial x} = \frac{-I_{cell}}{A_{cell} \times \sigma_{s,eff}}, \quad x = \{0, L\} \quad (19)$
$j^{tot} = j^{Li} + j^{DL} \quad (13)$	$\frac{\partial \phi_s}{\partial x} = 0, \quad x = \{\delta_{el,a}, L - \delta_{el,c}\} \quad (20)$
$j^{Li} = a_s i_0 \left( \exp \left( \alpha \frac{\eta F}{RT} \right) - \exp \left( (\alpha - 1) \frac{\eta F}{RT} \right) \right) \quad (14)$	$\frac{\partial \phi_s}{\partial x} = 0, \quad x = \{0, L\} \quad (21)$
$i_0 = k F c_e^\alpha (c_{max} - c_s) a_s^{1-\alpha} \quad (15)$	

For a complete set of equations see refs. [39,41].  $L$  denotes the full cell thickness and,  $\delta_{el,a}$  and  $\delta_{el,c}$  denote the layer thickness of anode and cathode, respectively.

response of the battery. For the investigated cells with local deviations, this is important, as even at constant current discharge, the local current density can change significantly at short time scales. In general, the model has a set of time-dependent state variables, such as solid and liquid phase concentrations ( $c_s$  and  $c_e$ , respectively), solid and liquid phase potentials ( $\phi_s$  and  $\phi_e$ , respectively), and the surface overpotential ( $\eta$ ) for both electrodes. The governing equations of the model and their boundary conditions are summarized in Table 1. From the states of the solid phase potential, the cell voltage can be derived as follows

$$U_{cell} = \phi_s(L) - \phi_s(0) \quad (22)$$

where  $L$  is the combined thickness of anode, separator, and cathode ( $\delta_{el,a} + \delta_{el,s} + \delta_{el,c}$ ). The effective liquid-phase diffusion coefficient ( $D_{e,eff}$ ) and the effective solid phase conductivity ( $\sigma_{s,eff}$ ) are determined by applying Bruggeman coefficients:

$$\sigma_{s,eff} = \sigma_s \times \varepsilon_s^\beta \quad (23)$$

All parameters, such as porosity, particle size, and shape, are assumed to be homogeneous within each electrode. Assuming a cell whose area ( $A$ ), in  $y$ - and  $z$ -directions, is huge compared with the anode's and cathode's thickness ( $\delta_{el,a}$  and  $\delta_{el,c}$ ) in  $x$ -direction, and assuming homogeneous parameters, there is no significant change in the mass transport in the second or third dimension,<sup>[40]</sup> that is

$$\frac{\partial c_e}{\partial y} = \frac{\partial c_e}{\partial z} = 0 \quad (24)$$

To reduce the number of independent uncertain parameters, the Nernst–Einstein equation is considered as follows

$$\sigma_e = \frac{F^2}{R} \times c_{Li} \times (D^+ + D^-) \quad (25)$$

which describes the relationship between liquid phase conductivity ( $\sigma_e$ ) and cation's and anion's liquid phase-diffusion coefficient ( $D^+$  and  $D^-$ ), respectively. This is a simplification compared with the concentrated solution theory of the classical Doyle–Newman Model.<sup>[40]</sup> However, it is of minor significance at the applied concentrations.

### 2.3.2. Governing Equations of the Area-Distributed Model

In contrast to the homogenized standard model, deviations of electrode properties along the cell area  $A_{cell}$ , i.e., in  $y$ - and  $z$ -directions, are addressed in the extended model, whereas a homogeneous structure is assumed along  $x$ -direction similar to that of the standard model. In addition to the investigated processes that cause mainly deviations in  $y$ - and  $z$ -directions, there are processes such as drying, which cause nonhomogeneities in the  $x$ -direction.<sup>[42,43]</sup> However, the consideration of deviations in 3D would require a full 3D model. This would not be beneficial to the sample-based PEM, due to its high computational cost. Hence, in this work, the focus is set on the deviations of electrode properties along the cell area.

Therefore,  $A_{cell}$  is divided into a finite number of sub-cells  $A_i$  of slightly different properties, for example, solid volume fraction ( $\varepsilon_{s,i}$ ) and electrode thickness ( $\delta_{el,i}$ ). For the stacked pouch in the experiments a sub-cell is equivalent to one compartment as illustrated in **Figure 4**. A complete list of all uncertain parameters is given in **Table 2**. Based on the assumptions in the standard model in Equation (24), and neglecting the resistance of the current collector, as it is small compared with the resistance of the electrodes, ( $\sigma_{Cu} = 58 \times 10^6 \text{ S m}^{-1} \gg \sigma_{C_6} = 0.11 \text{ S m}^{-1} \gg \sigma_{NMC} = 68 \times 10^{-3} \text{ S m}^{-1}$ ) (see refs. [44–46]), the liquid-phase diffusion in the sub-cells can be calculated separately in one single 1D-scheme per sub-cell. This assumption leads to a

parallel arrangement of the sub-cells with independent diffusion processes, but with a uniform voltage and coupled currents.

There are a few models of battery systems introduced in the literature considering cell-to-cell deviations. For instance, Dubarry et al. simulated a battery pack consisting of equivalent circuit models (ECMs).<sup>[47,48]</sup> Kenney et al. applied a serial set of SPMs to simulate cells stacked in sequence.<sup>[12]</sup> However, the scope of these models was to predict aging or to control processes in battery management systems, and it is far from the scope of this work, which is the quantification of deviations of electrode properties along the cell area and the assessment of the feasibility of the applied PEM for this purpose. In addition, the P2D model applied in this work is superior to an ECM

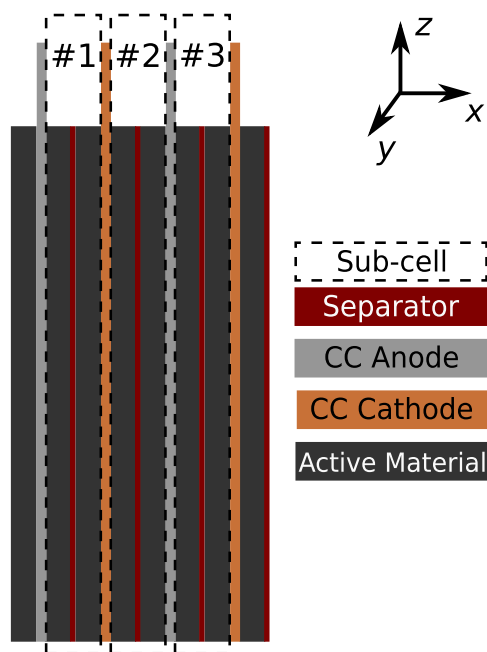


**Figure 4.** Model domains of the extended model.

or an SPM in terms of physical product parameters and validity for a wide C-rate range.

In addition to the states of the  $N$  in parallelly coupled P2D models, the current of each area ( $I_i$ ) is an additional state variable. The sub-cell currents have to satisfy two conditions: conservation of charge and equality of voltage in all sub-cells

$$0 = I_{\text{total}} - \sum_{k=1}^N I_k \quad (26)$$

$$0 = U_{\text{cell}} - U_k, \quad k = 1, \dots, N \quad (27)$$

Using the equation introduced above, it is possible to discretize a cell in sub-cells with different electrode properties that can be varied independently for both electrodes. Data of both models are analyzed using Matlab 2016a and run on a CentOS Linux desktop PC @3.40 GHz and 32 GB of RAM.

#### 2.4. Cell Parameters of the 9 A h Pouch Cell

The method introduced above is applied to a LIB containing graphite ( $\text{Li}_x\text{C}_6$ ) and  $\text{Li}(\text{Ni}_{1/3}\text{Co}_{1/3}\text{Mn}_{1/3})\text{O}_2$  (NCM) as anode and cathode, respectively. Model parameters are obtained from ref. [41] own measurements or are determined via parametrization of the model, and they are presented in Table 2.

Layer thickness and area specific weight are measured as discussed in Section 3, the specific capacity is derived from the open cell potentials (OCP) measurement, and the mean porosity is derived from  $d_{\text{el}}$ ,  $f_{\text{el}}$ , the composition of the electrode, and the densities of its components. The calculated porosity is slightly higher than those measured by applying a mercury intrusion technique<sup>[27]</sup>, but it is believed to be more accurate.

For the estimation of the homogeneous parameters, as shown in Table 2, a least square curve fitting technique is used

$$X^*:F(X^*) = \min_{X \in \mathbb{R}^N} |F(X)| \quad (28a)$$

**Table 2.** Cell parameters used in the applied model.

Parameter	Symbol	Unit	Anode	Separator	Cathode
Layer thickness <sup>m,u</sup>	$\delta_{\text{el}}$	$\mu\text{m}$	55.25	20.0	60.0
Porosity <sup>m,u</sup>	$\varepsilon_e$	—	0.35	0.50	0.40
Diffusion coefficient <sup>a</sup>	$D_e$	$\text{m}^2\text{s}^{-1}$	$7.15 \times 10^{-9}$	$7.15 \times 10^{-9}$	$7.15 \times 10^{-9}$
Diffusion coefficient <sup>a</sup>	$D_s$	$\text{m}^2\text{s}^{-1}$	$9.35 \times 10^{-15}$	—	$1.10 \times 10^{-12}$
Particle size <sup>m,u</sup>	$R_p$	$\mu\text{m}$	11.5	—	5.5
Specific capacity <sup>m,u</sup>	$\Delta c_{\text{max}}$	$\text{molL}^{-1}$	24.9	—	25.4
Electronic conductivity <sup>a,u</sup>	$\sigma_s$	$\text{mSm}^{-1}$	20.4	—	9.9
Exchange current density <sup>a,u</sup>	$i_0$	$\text{Am}^{-2}$	1.47	—	198
Transference number <sup>l</sup>	$t_p$	—	0.24	0.24	0.24
Charge transfer coefficient <sup>l</sup>	$\alpha$	—	0.5	—	0.5
Double layer capacity <sup>l</sup>	$C_{\text{DL}}$	$\text{Fm}^{-2}$	0.2	—	0.2

Given as mean value, if uncertain. The separator is assumed to have no uncertainties.  $m$ , measured;  $u$ , uncertain parameter;  $a$ , adjusted;  $l$ , taken from ref. [41].

$$F(X) = \sum_j^m \left( \sum_{k=1}^n (U_{\text{sim}}(C_k, X, t) - U_{\text{exp}}(C_k, t))^2 / U_{\text{max},j}^2 + \sum_{k=1}^n (C_{\text{sim}}(U_k, X) - C_{\text{exp}}(U_k))^2 / C_{\text{max},j}^2 \right) \quad (28b)$$

Here, the simulated capacity ( $C_{\text{sim}}$ ) and cell voltage ( $U_{\text{sim}}$ ) are compared with the experimentally measured capacity ( $C_{\text{exp}}$ ) and cell voltage ( $U_{\text{exp}}$ ) at  $m$  C-rates at  $n$  equidistant points ( $C_k$  and  $U_k$ , respectively). Both differences are normalized to the maximum capacity and respective voltage of simulation and experiment at the corresponding C-rate. The consideration of deviations in the directions of capacity and voltage becomes necessary in areas with a very low or very high slope ( $dU/dC$ ). For instance, at the end of discharge, where  $dU/dC$  is steep, a marginal shift of the onset of the diffusion limitation would lead to a significant deviation regarding the cell voltage. In contrast, Equation (28b) considers the impact of the deviations in  $C$ - and  $U$ -directions on the numerical fit and enables a solution  $X^*$  that provides a good fit for the whole capacity range. The resulting values are summarized in Table 2.

In this work, a parameter is uncertain, if it is affected by the deviations of the investigated process steps: coating and calendaring. This includes layer thickness and porosity, but excludes all intrinsic parameters such as the solid-phase diffusion coefficient. In contrast, the solid phase conductivity is a macroscopic effective parameter that is affected, for example, by the CB-binder matrix, which in turn is affected by coating and calendaring. Eventually, this classification leads to similar uncertain parameters as commonly shown in the literature, see Section 1. If not noted elsewhere, all uncertain parameters  $X_i$  are assumed to be independent and normally distributed with  $X_i = \bar{X}_i \pm 5\%$ . For deviations observed in the literature, see Section 1. For deviations observed at the investigated 9 A h cell, see Section 4.1.

The OCP depend on the normalized concentration ( $\tilde{c} = c/c_{\text{max}}$ ) of the exemplary cell as described by the following equation

$$OCP_a(\tilde{c}) = k_1 + k_2\tilde{c} + k_3\tilde{c}^{0.5} + k_4\tilde{c}^{1.5} + k_5 \exp(k_6(k_7 - \tilde{c})) + k_8 \exp(k_9(k_{10} - \tilde{c})) + k_{11} \exp(k_{12}(k_{13} - \tilde{c})) + k_{14}(k_{15} + \tilde{c})^{-1} \quad (29)$$

for the anode and by

$$OCP_c(\tilde{c}) = k_1\tilde{c}^6 + k_2\tilde{c}^5 + k_3\tilde{c}^4 + k_4\tilde{c}^3 + k_5\tilde{c}^2 + k_6\tilde{c} + k_7 \exp(k_8\tilde{c}^{k_9}) + k_{10} \quad (30)$$

for the cathode, respectively. Equations, similar to those of Smith and Wang,<sup>[49]</sup> are used and the coefficients are determined by a least square fit on the experimental data from the cells as described in Section 3. The coefficients are listed in Table 3.

### 3. Experimental Section

#### 3.1. Electrode and Cell Preparation

For the electrode production, commercially available NCM, with a theoretical capacity of 165 mAh g<sup>-1</sup>, and surface-modified

**Table 3.** Coefficients of the empirical half-cell potential functions.

Coefficient	Anode	Cathode
$k_1$	8.0391 V	3.1058 V
$k_2$	5.0822 V	-9.5098 V
$k_3$	-12.561 V	10.372 V
$k_4$	0.4484 V	-5.0932 V
$k_5$	-0.0962 V	1.9426 V
$k_6$	15.001	-1.4960 V
$k_7$	0.1684	5.9019 V
$k_8$	-0.4599 V	$-1.3812 \times 10^{-5}$
$k_9$	2.3166	415.09
$k_{10}$	0.5856	-1.5383 V
$k_{11}$	-0.9575 V	-
$k_{12}$	2.4033	-
$k_{13}$	0.5124	-
$k_{14}$	-0.0114 V	-
$k_{15}$	0.03173	-

graphite (SMG), with a theoretical capacity of 360 mAh g<sup>-1</sup>, were used on the cathode and anode sides, respectively. The NCM has an average particle size of  $\approx 11 \mu\text{m}$  and a surface area Brunauer–Emmett–Teller (BET) of  $\approx 0.25 \text{ m}^2 \text{ g}^{-1}$ . The SMG has an average particle size of  $\approx 23 \mu\text{m}$  and a surface area (BET) of  $\approx 2.1 \text{ m}^2 \text{ g}^{-1}$ . In addition, CB with a surface area (BET) of  $\approx 62 \text{ m}^2 \text{ g}^{-1}$ , conductive graphite (G) with a surface area (BET) of  $\approx 16 \text{ m}^2 \text{ g}^{-1}$ , and polyvinylidene fluoride (PVDF) were added to both electrodes as conducting additives and binder, respectively. The compositions of the solids in the suspensions are listed in Table 4.

All solids were dry-mixed in a planetary mixer (PMH-10, NETZSCH Corp.) for 5 min to obtain a homogeneous mixture. N-Methyl-2-pyrrolidone (NMP) as a solvent was added after the dry mixing step to obtain a suspension of 55 and 45 wt% for anode's and cathode's slurry, respectively. The suspensions were mixed for 60 min and degassed under vacuum for another 30 min using the planetary mixer. In the next step, aluminum or copper foil was coated on one side using a pilot scale coater (LabCo, Kroenert Corp.) with a dry coating weight of  $16.88 \pm 0.12$  and  $8.40 \pm 0.06 \text{ mg cm}^{-2}$  on cathode and anode sides, respectively.

Dry coating weights were obtained by ultrasonic measurements (USM-200 Array, MeSys Corp.) after the drying process of the continuous coater. This device uses an oscillating sensor with a measuring frequency of 100 Hz continuously crossing the dry electrodes. In the calendaring step, the electrodes were compressed to the densities of  $1.5 \text{ g cm}^{-3}$  at the anode and  $2.8 \text{ g cm}^{-3}$

**Table 4.** Recipes for cathode and anode suspension. Listed are the amounts of solid contents in wt%.

	PVDF	CB	G	NCM, respectively SMG
Anode	5	2	2	91
Cathode	4	4	2	90

at the cathode. Electrode density was calculated before and after calendring of the electrode using the coating weight and electrode thickness with a tactile measurement for every 5 m of the electrode. Double-sided coated electrodes were cut out in sheets of 11.0 cm x 15.0 cm for the anode and 10.5 cm x 14.5 cm for the cathode, using a laser beam. In the next step, these electrodes were assembled to pouch full cells with 15 layers of cathode-separator-anode-configuration according to a cell capacity of about 9 Ah and filled with electrolyte with a composition of ethylene carbonate (EC)/dimethyl carbonate (DMC)/ethyl methyl carbonate (EMC) (1:1:1) + 1 M LiPF<sub>6</sub> + 2% vinylene carbonate (VC) + 3% cyclohexyl benzene (CHB). The cells were produced in five batches. A detail description of the manufacturing process and a comprehensive experimental investigation of the pouch cell batch production are given in ref. [50].

For OCP measurements and model parametrization, the electrodes with a diameter of 18 mm were manually punched out of the large sheets and assembled in a three-electrode setup with a lithium metal ring as reference (PAT-Cell, EL-CELL GmbH).

### 3.2. Electrochemical Cell Characterization

Formation of pouch cells and EL-Cells was conducted at 0.1 C for the two consecutive cycles. C-rate tests were conducted for EL-Cells at 0.2, 0.5, 1, 2, and 3 C and for pouch cells at 0.1, 1, and 2 C. All experiments were conducted in temperature chambers at 25 °C. For OCP measurement, an EL-cell was discharged incrementally from 4.2 to 2.9 V in steps of 0.05 V and relaxation was maintained till  $dU/dt \leq 0.2 \text{ mV h}^{-1}$ . The cell resistance of the pouch cells was determined by a pulsed discharge of 1 C for 1 s at 50% SOC. In ref. [51], it is shown that the performance of the EL-cell is in good accordance with the performance of the stacked pouch cell. Hence, the model parameterized using the three-electrode setup in this work should also be able to simulate the stacked pouch cell.

## 4. Results and Discussion

The outline of this section is as follows. Deviations of experimental cells and product parameters are summarized. Next, local SA and global SA are carried out. The global SA applying the nested PEM is assessed in comparison with the first-order SA, and the influence of sub-cell level deviations is assessed, where appropriate.

### 4.1. Deviation of Product Parameters

As shown in **Figure 5a**, the layer thickness of the evaluated cells has a normal distribution with the standard deviations of 1.2% and 0.88% for anode and cathode, respectively.<sup>[50]</sup> The resulting cell capacity of the pouch cells at different C-rates is shown in **Figure 5b**. With increasing C-rate, the standard deviations are 3.4%, 4.3%, and 4.6%. However, the number of samples is too small to evaluate the shape of the distribution, as the lot-to-lot deviation is large compared with the cell-to-cell deviation. This causes a significant non-normal distribution.

The measured open-cell voltage (OCV) at 50% SOC is  $3.6956 \pm 0.0055 \text{ V}$ . The deviations are quite small, which is reasonable as the OCV is only affected by the thermodynamic

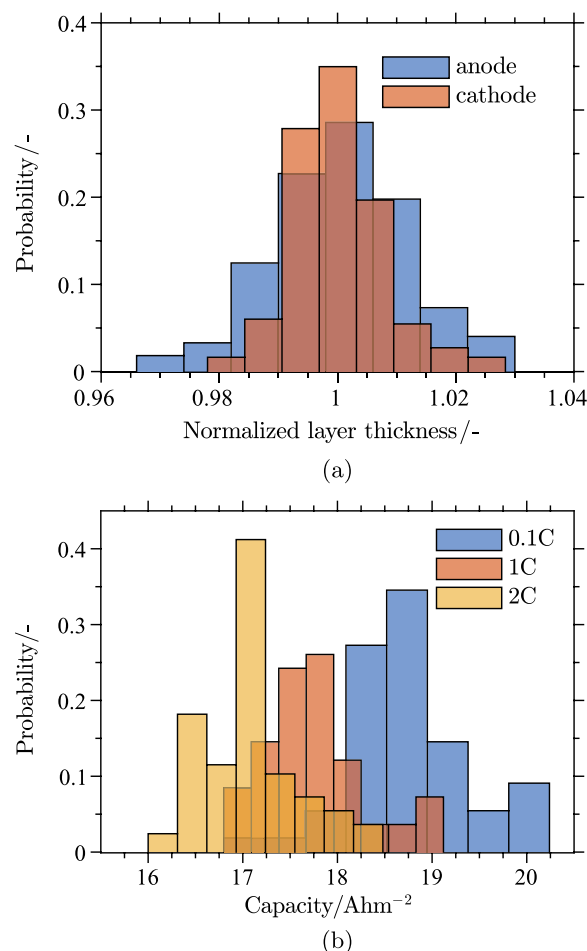


**Figure 5.** Product properties of evaluated pouch cells from ref. [50]: a) Normalized layer thickness of anode and cathode (Anode: 273 sample points; Cathode: 183 sample points). b) Capacity at different C-rates of 55 pouch cells.

properties of the active material. The experimental ohmic cell resistance is  $12.5 \pm 4.0 \text{ m}\Omega$ . The standard deviation of this parameter is 32%, which is high compared with the other investigated parameters. This could be due to a high sensitivity of the contacting of the stacked electrode sheets or due to the contacting of the particle layer to the current collector.

The deviations of the layer thickness and discharge capacity of the evaluated cells are in the range of deviations in the literature discussed in Section 2.4. In addition, it should be noted that the standard deviation of the discharge capacity is significantly higher than that of the layer thickness of anode and cathode, respectively.

In **Figure 6a**, the discharge curves of EL-Cells (solid lines) at 0.5–3 C and simulated C-rate tests (dashed lines) are shown. It can be seen that there is a very good agreement between simulations and experimental data for the investigated range from 0.2 to 3 C.

In **Figure 6b**, the UP is compared between simulation (solid lines) and experiment (grey area and histograms, respectively). For the MC simulations, deviations as measured and listed at



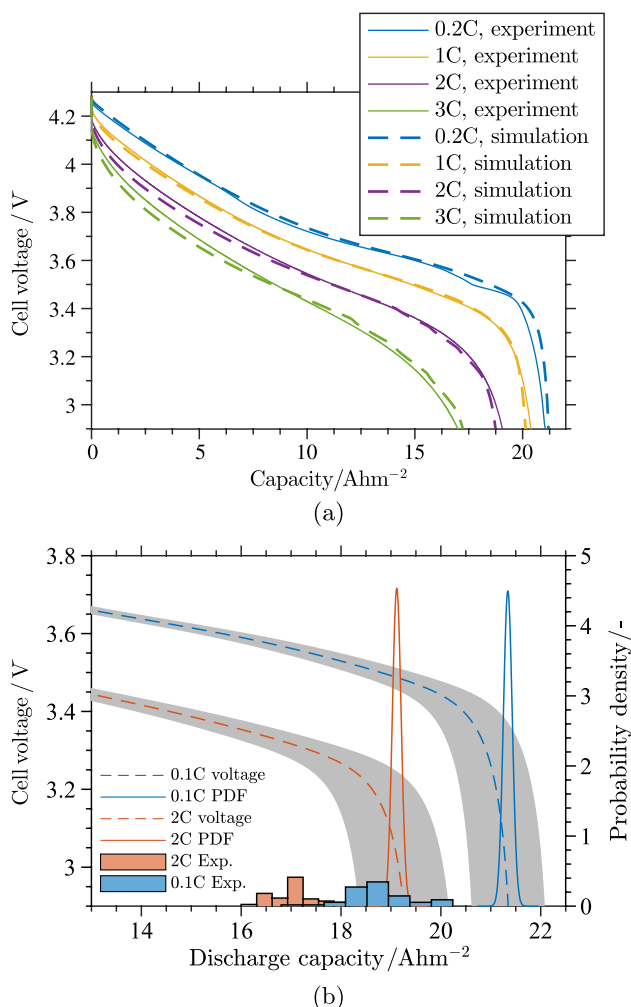


**Figure 6.** Validation of the model considering EL-Cell measurements and the standard deviation of the large-format pouch cells. a) Experimental (solid lines) and simulated (dashed lines) C-rate tests of an EL-Cell. b) Extract from simulated C-rate test of an EL-Cell. The grey area is the confidence interval calculated from Figure 5b applied to the simulation data of the model, parameterized to EL-Cells. MC sampling with 5000 sample points. Histogram shows experimental discharge capacity of pouch cells as shown in Figure 5b.

the beginning of this section are  $\pm 1.2\%$  and  $\pm 0.88\%$  for the layer thickness of anode and cathode, respectively. As the area-specific weight is held constant during the manufacturing process, it is assumed to be constant, which leads to a deviation of porosity that is linearly correlated to the layer thickness. To model the uncertainty of the cell resistance, the reciprocal electrolyte conductivity and the reciprocal electrolyte diffusion coefficient are varied by  $\pm 32.0\%$ . All other parameters are set constant to investigate whether  $d_{el,i}$ ,  $\epsilon_i$ , and  $R_{cell}$ , as easily measurable quantities, could provide sufficient information to understand and quantify the process deviations. The discharge capacity shows a standard deviation of 0.45% at 2.9 V and 0.5% at 0.1 and 2 C. While the increase in the deviation with increasing C-rate is significant in the simulations (+11.1%) and in the experiments (+35.3%), the width of the simulated distribution with a deviation of  $\pm 0.45\%$  to

$\pm 0.5\%$  is significantly lower than that in the experiments with a deviation of  $\pm 3.4\%$  to  $\pm 4.6\%$ . The displacement between histogram and grey area is due to the different cell formats. The histogram is based on stacked pouch cells, while the grey area is the projection of the deviation of the pouch cells on the smaller laboratory cells (PAT cells), which allows comparison with the simulation data, as the model is parameterized and validated with labor cells that provide a three-electrode setup. The difference between predicted and measured deviations suggest that not all relevant uncertain parameters in the cell production have been identified. Furthermore, deviations in the cell assembly and the electrolyte injection are not quantified yet as imaging the influences of, for example, electrode stacking would require a full-order electrochemical 3D model. Furthermore, it is likely that there are process deviations that affect parameters, which are generally not covered by the classical Doyle–Newman model. Furthermore, it is possible that the sensitivity of the mathematical battery model to its parameters does not fit the sensitivity of the real battery to its parameters; nevertheless, the model is feasible to describe the discharge performance of the reference cell accurately.

Based on these findings, in the further simulations, additional uncertain parameters are considered, which are assumed to be also affected by process uncertainties in the production.

## 4.2. Parameter SA

Next, a global first-order SA is carried out to investigate the influence of the different product parameters on the cell capacity. This allows a quantification of the effect that an input variable such as the layer thickness has on an output variable such as the discharge capacity. However, this approach is not feasible to quantify any interactions between parameters. To evaluate the influence of all uncertain input parameters, MC simulations are conducted. Using the PEM, a global SA is conducted to show the interactions between uncertain parameters. This method could be feasible to substitute the combination of first-order SA and MC simulations for UP. In that case, using the PEM could reduce the computational cost for UQ significantly. For simplification, an input parameter is denoted as sensitive if there is an output parameter that is sensitive to this input parameter.

### 4.2.1. First-Order SA

A global first-order SA is carried out by varying each parameter consecutively, whereas all other parameters are kept constant at the values presented in Table 2. The varied parameters are layer thickness ( $\delta_{el}$ ), porosity ( $\epsilon_e$ ), particle size ( $R_p$ ), and specific capacity ( $\Delta c_{max}$ ) of anode and cathode. Figure 7a–c shows the resulting discharge capacities at 0.2, 1, and 3 C, respectively. Parameter variations are  $\pm 10\%$  to investigate a range slightly larger than the expected range discussed in Section 2.4. In general, the slope of these graphs is a measure of sensitivity. In this figure, the graphs of variations of the effective electrical conductivity are not shown, as this parameter is insensitive for all C-rates for the investigated cell.

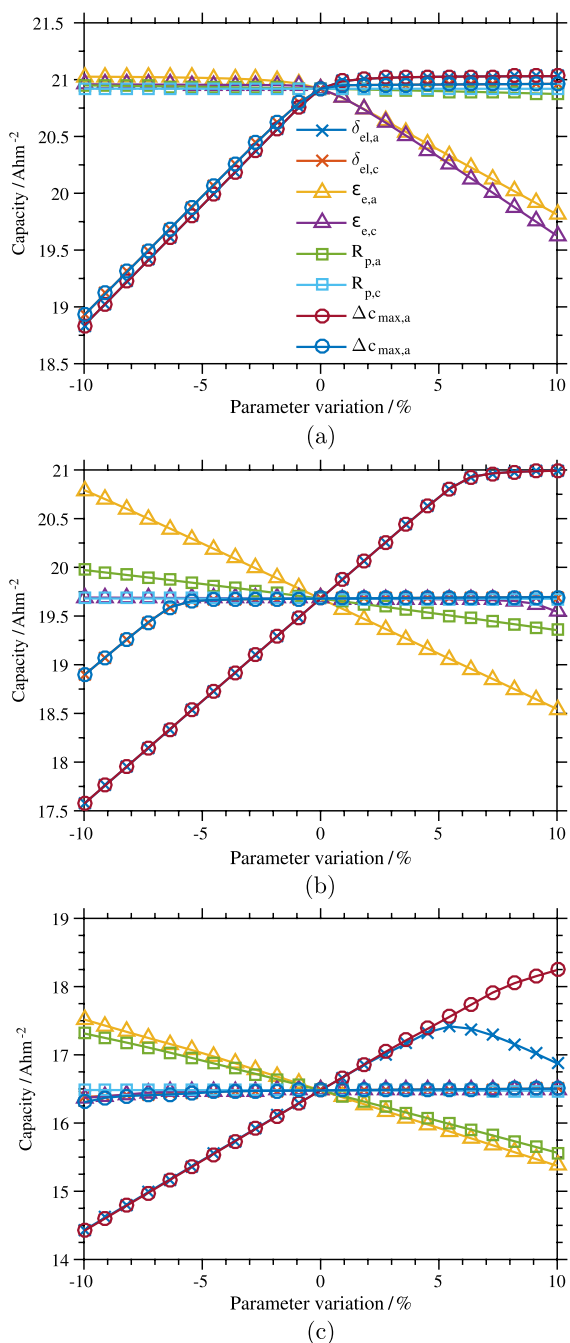


**Figure 7.** First-order SA: Discharge capacity versus variation of parameter. a) 0.2 C, b) 1 C, and c) 3 C. The legend in Figure 7a is valid for all three plots.

Sensitive parameters at 0.2 C are the porosity, specific capacity, and layer thickness (see Figure 7a). A change in those parameters causes a linear decrease in the discharge capacity, but there is no significant increase compared with the cell with reference parameters. This is attributed to the good balancing of the electrodes and to the fact that the cell performance is solely limited by the electrode with lower theoretical capacity ( $C_{theo,i}$ )

$$C_{theo} = \min(\{C_{theo,a}, C_{theo,c}\}) \quad (31a)$$

$$C_{theo} = A_{cell} \times \min(\{\epsilon_{s,a} \times \delta_{el,a} \times \Delta c_{max,a}, \epsilon_{s,c} \times \delta_{el,c} \times \Delta c_{max,c}\}) \quad (31b)$$

as kinetic effects have little influence at 0.2 C. As such, the particle sizes  $R_{p,i}$  are also insensitive. The slopes of the graphs of both electrodes are similar. The occurrence of the transition between sensitivity and insensitivity of many parameters at almost exactly zero parameter variation illustrates the precise balancing of the cell for the operation at low cell currents.

As shown in Figure 7b, at 1 C, the performance becomes sensitive to the particle size of the anode, whereas the cathode's layer thickness and specific capacity have an effect only when they are decreased to more than  $-5\%$ . In this range, there is again a linear effect on the discharge capacity. In contrast, the anode's layer thickness and specific capacity are sensitive till a threshold of about  $+5\%$  after which they become insensitive. The sensitivity of the cathode's porosity is negligible at this C-rate. As moderate changes of cathode parameters cannot alter the cell performance, the discharge capacity at 1 C is not limited by the capacity of the cathode. The anode layer thickness ( $\delta_{el,a}$ ) and specific concentration ( $\Delta c_{max,a}$ ) of the anode show a similar sensitivity as  $\delta_{el,c}$  and  $\Delta c_{max,c}$  in their sensitive range, respectively. For the investigated range of porosity and particle size of the anode, the system behaves linearly. The sensitivity of the performance to the anode's particle size indicates a limitation of the cell by diffusion processes in the active material of the anode. In summary, kinetic effects become significant as indicated by the increasing sensitivity to the particle size.

The first-order sensitivities at 3 C are similar to those at 1 C. The sensitivity to the particle size ( $R_{p,a}$ ) increases while the cathode, in general, becomes less sensitive. A noteworthy feature is a distinguished maximum at an anode layer thickness of about 105%. This indicates a limitation due to charge or mass transport in the electrolyte phase along the cell area. The decrease in the cathode's sensitivity and the distinct maximum of the graph of  $\delta_{el,a}$  suggests higher sensitivities of the anode to high C-rates compared with the cathode. For both electrodes, some graphs show that nonlinear behavior and transitions between linear areas with different slopes become smoother than those at 0.2 C as shown in Figure 7a. For 3 C, this indicates an interaction of different limitations that decrease the cell performance simultaneously.

From Figure 7a–c, four types of parameters are derived: 1) in- or minor-sensitive parameters; 2) parameters sensitive in the entire parameter range (linear and nonlinear); 3) parameters sensitive till a certain threshold; and 4) parameters sensitive from a certain threshold. The classification of parameters could be used for an advanced optimization or balancing process that considers limitations at different C-rates. In this work, in the following UQ, it is considered that the kind of parameter sensitivity influences the shape of the PDF of the output parameters of the investigated system.

Regarding the design of batteries, the conducted global first-order SA shows a need for a model-based balancing approach to set up a battery cell that is well balanced at all applied C-rates, as the limitation changes with the C-rate. This will also help to

prevent lithium plating. Regarding the UQ of the product parameters of an LIB, the nonlinearity of the system indicates that the discharge capacity of the battery is to a certain extent not normally distributed. For a significant asymmetry of the capacity, the PEM could fail to reconstruct the PDF. Because of this limitation, MC simulations were used to investigate the symmetry of the system output in the following section.

#### 4.2.2. UQ Applying MC Simulations

To evaluate the shape of the PDF regarding asymmetry, from **Figure 8**, the PDF of the discharge capacities at 0.2, 1, 3, and 4 C were determined. They are determined from MC simulations with 10 000 sample points considering the 11 uncertain parameters, marked as uncertain in Table 2, with  $X_i = \bar{X}_i \pm 5\%$ , independent of the deviations determined experimentally. A C-rate of 4 C is simulated additionally, to confirm the hypotheses of an increase in the standard deviation with increasing C-rate.

The corresponding standard deviations are 3.20%, 3.20%, 3.88%, and 7.46% for 0.2, 1, 3, and 4 C, respectively. The increase in the standard deviation with increasing C-rate could be due to a change in the sensitivity of the product parameters depending on the C-rate and could indicate an interaction of different partially limiting processes and parameters. This leads to the conclusion that there is a need for a physics-based model to reconstruct process-to-product dependencies and thus to optimize the battery production. In general, it seems impossible to conclude any nonlinear dependencies from a normally distributed output.

#### 4.2.3. Global SA Applying the PEM

As illustrated in the first-order SA, the system is significantly nonlinear due to the transition of limitations between different processes in the electrodes. Therefore, under the condition of high nonlinearity or nondifferentiability, the PEM is not a suitable method. In fact, for the parameters varied as shown in **Figure 8**, it provides mathematically incorrect Sobol indices at 0.2 C. As this operational conditions showed the most nondifferential behavior as shown in **Figure 7a**, it is assumed that the

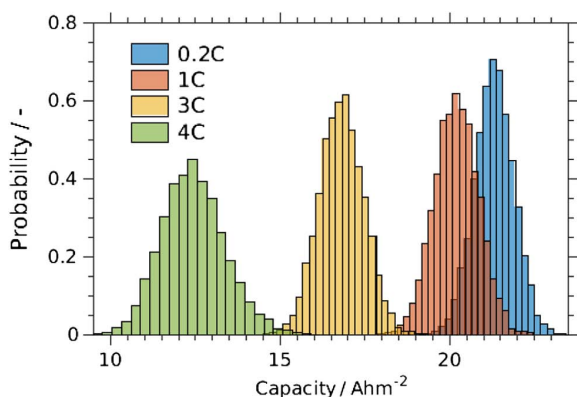


**Figure 8.** Histogram of the discharge capacity of 10 000 simulated discharge capacities at 1, 3, and 4 C considering 11 uncertain parameters with  $X_i = \bar{X}_i \pm 5\%$ . Sample points are chosen randomly (MC Approach).

failure of the PEM is due to the nondifferentiability of the model in this aspect. However, it shall be used to show sensitivities and interactions independently of the given set of electrodes. To enable this and to overcome the limitations of the PEM discussed in Section 2.2, the PEM is applied on two different cell setups: one with a 10% increased layer thickness of the anode ( $\delta_{el,a} = 60.78 \mu\text{m}$ ) and one with a 10% increased layer thickness of the cathode ( $\delta_{el,c} = 66.0 \mu\text{m}$ ). Due to this change in the layer thickness, the cells are not in the point of the nonlinearity at 0.2 C, as shown in **Figure 7a**. Comparing the sensitivities of both cells can also enable more general conclusions which go beyond the influence of the simulated cell geometry.

C-rate tests are simulated for the two cells at 0.2, 1, and 3 C. The evaluated output parameters are the discharge capacity and the cell voltage after discharging 50% of theoretical capacity at the corresponding C-rate.

Results of these simulations are summarized in **Figure 9**, where Sobol Indices and Total Sobol Indices are shown for the ten uncertain product parameters for the influence on discharge capacity and cell voltage at 50% SOC and at 0.2 and 3 C. The number of uncertain parameters is reduced by one, as one electrode is over-designed and kept constant to overcome the limitations of PEM regarding the differentiability of the system's output. Each peak indicates a sensitive parameter at the given performance criterion.

Obviously, the cell performance is sensitive to the cell area ( $A_{cell}$ ) and layer thickness of the nonadjusted electrode ( $\delta_{el,i}$ ), whereas it is insensitive to electrical conductivity of the solid phase ( $\sigma_s$ ) for both electrodes. Interactions between parameters are marginal, as there is no significant difference between Sobol Indices and the corresponding Total Sobol Indices.

Comparison of **Figure 9b,d** shows that with increasing C-rate, the anode particle size ( $R_{p,a}$ ) becomes sensitive, which is in good accordance with the first-order SA. In addition, **Figure 9b,d** shows that the cell capacity is sensitive to the anode, characterized by  $\epsilon_{e,a}$  and  $d_{el,a}$ , as the cathode's layer thickness was increased, whereas the cell voltage at 50% SOC is sensitive to the parameters of the cathode. This is related to the higher slope ( $dU/dC$ ) of the OCP curve of the cathode compared with the anode. Consequently, a change in the concentration in cathode leads to a significant change in the voltage, and the limitation at the end of discharge is related to the anode.

From **Figure 9a,c**, it is clear that the sensitivities of cell voltage at 50% SOC and the discharge capacity are similar. But at 3 C, the cell voltage at 50% SOC becomes sensitive to the anode particle size, whereas the discharge capacity becomes sensitive to the anode's porosity, as compared with that at 0.2 C.

In general, the most sensitive parameters are the porosity ( $\epsilon_{e,c}$ ) and the specific capacity ( $\Delta c_{max,c}$ ) of the cathode, and the layer thickness and cell area of both cathode and anode. The results of the first-order SA for the cell with reference parameters already showed a strong sensitivity of the battery on the anode. The global SA of a cell with slightly altered electrode layers showed additionally a sensitivity of the cell voltage to the electrode with the steeper OCP curve independently of the specific cell geometry. In the development of commercial battery cells, this has to be considered in the balancing and in the set of quality requirements. Thus, regarding large-scale process deviations, the cathode should be produced with higher quality requirements.

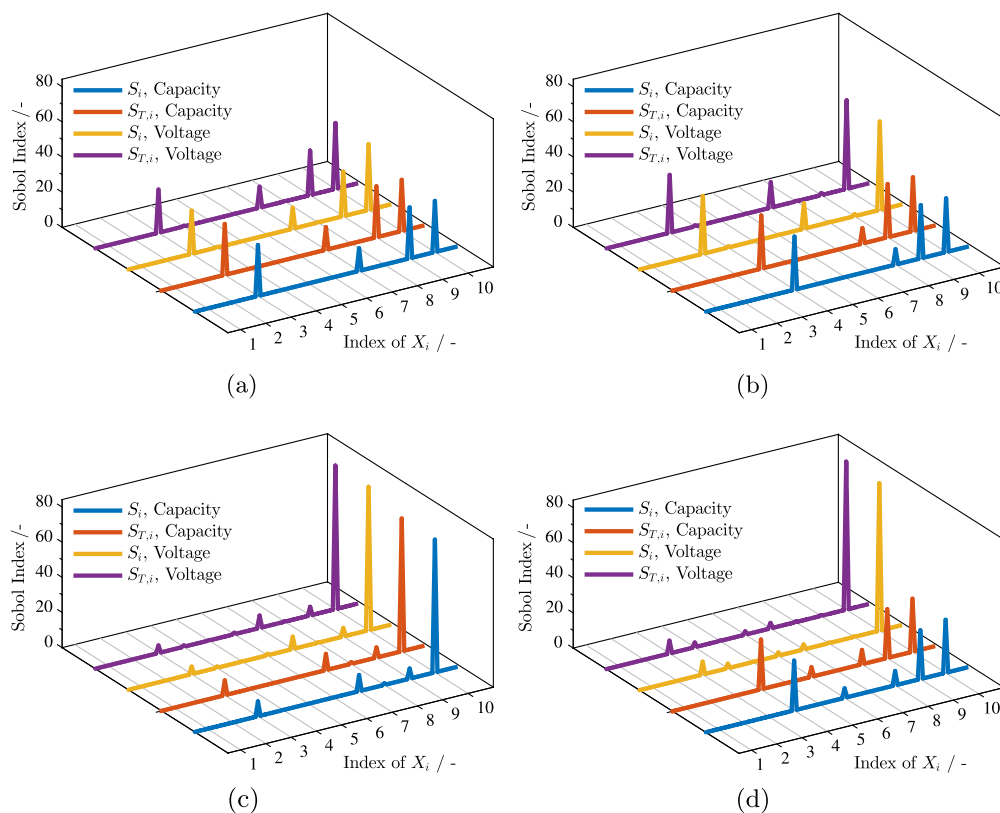


**Figure 9.** Global SA for a cell with a)  $\delta_{el,a} = 60.78 \mu\text{m}$  at 0.2 C, b)  $\delta_{el,c} = 66.00 \mu\text{m}$  at 0.2 C, c)  $\delta_{el,a} = 60.78 \mu\text{m}$  at 3 C, and d)  $\delta_{el,c} = 66.00 \mu\text{m}$  at 3 C. Ten uncertain parameters  $X_i$  are considered: 1)  $\sigma_{s,c}$ , 2)  $\sigma_{s,a}$ , 3)  $\Delta c_{max,c}$ , 4)  $\Delta c_{max,a}$ , 5)  $R_{p,c}$ , 6)  $R_{p,a}$ , 7)  $\epsilon_{e,c}$ , 8)  $\epsilon_{e,a}$ , 9)  $\delta_{el,i}$ , and 10)  $A_{cell}$ . The layer  $\delta_{el,i}$  denotes the layer thickness of the non-adjusted electrode.

This supports the common practice to have a slightly oversized anode, similar to the cell simulated in Figure 9a,c. At this instance, quality requirements for the cathode should consider porosity, for example, whether the quality is affected by calendaring, and the intrinsic parameters of the active material that are affected by the supplied material. However, it should be noted that these guidelines are sensitive to the respective cell and application.

#### 4.3. Assessment of the Nested PEM

In the UQ in this work, two methods have been applied. First, a first-order global SA is combined with MC simulations. Second, the nested PEM introduced in ref. [36] is applied to calculate the Sobol Indices. These approaches differ in terms of information obtained about the investigated system, the computational cost, and the limitations regarding nondifferentiability of the system.

Comparing Figure 9 with Figure 7a–c shows that both SA approaches are feasible to reveal sensitive parameters. C-rate dependency of the sensitivity of some parameters could also be quantified using both methods.

In addition to the information obtained from the first-order SA, the nested PEM provided the Total Sobol Indices quantifying the interactions between different uncertain parameters. For the investigated system, deviations and sensitivities seem to

be insufficiently high to obtain noticeable interactions. A general lack of interactions is unlikely for the investigated system, as Equation (31b) provides a lumped approximation of the dependency between cell parameters and cell capacity at a low C-rate. Therefore, it cannot be excluded that the PEM might have a limitation regarding the resolution of minor interactions.

The PEM assumes a normal distribution of the output. In contrast, the MC simulations provide additional information regarding the shape of the output distribution. However, as the output is quite symmetrical for the validated operational range of C-rates of 0.2–3 C, this advantage is of no practical relevance in the present investigated case. It, however, may become relevant for another cell chemistry or different operational conditions.

While the results of both approaches are similar, there is a significant difference in the required number of sample points. For the conducted analysis, ten uncertain parameters are considered in Section 4.2 and from 5 to 30 in Section 4.4. While the PEM requires  $2n^2+1$  sample points, for example, for MC simulation with 11 uncertain parameters, 10 000 sample points are chosen in comparison with the required 243 of the PEM. As such, the nested PEM provides comparable results with significantly lower computational costs compared with the approach of applying MC simulations. A drawback of the PEM is its sensitivity to the differentiability of the investigated system. But this drawback could be avoided if slightly adjusted cells

are investigated, as shown in Section 4.2, or a C-rate of 1 or higher is considered, see Figure 7b,c compared with Figure 7a.

#### 4.4. Investigation of Sub-Cell Level Deviations

In this section, the PEM and the extended model, as introduced in Section 2.3, are used to quantify the effect of sub-cell deviations. Five sub-cells, parallel to each other, are considered in the extended model to simulate deviations in the cell due to the production process. Six independent uncertain parameters ( $X_i = \bar{X}_i \pm 5\%$ ) per sub-cell are considered:  $\delta_{el,j}$ ,  $\epsilon_{e,j}$ , and  $\Delta C_{max,j}$ , where  $j$  indicates anode and cathode, respectively. This results in a total of 30 uncertain parameters. The choice of parameters is based on the high sensitivity of the cell performance to those six parameters, described in Section 4.2. For comparison with the model considering sub-cell deviations, the same model is used with five identical sub-cells, thus containing only six uncertain parameters in total. Consequently, the latter model's discharge curves and PDFs are identical to the results of the standard model.

In **Figure 10**, the discharge curves of the extended model at 0.2 and 3 C and the PDFs of both models at 0.2 and 3 C are shown. The PDFs are determined using the PEM. The discharge curves represent the reference cell with five identical sub-cells and standard parameters. This reference simulation is the same for both models as only the expectation values are used. See the first sample point ( $\xi_1$ ) in Equation (2).

Comparing both models, there is a marginal shift of the determined mean discharge capacity from 15.93 and 15.95  $\text{A m}^{-2}$  with and without consideration of sub-cell level deviations, respectively, and a significant shrinking of the confidence interval for the model considering sub-cell level deviations,  $\sigma = 0.066$  compared with 0.133 for the standard model. Note that the mean discharge capacity is slightly smaller than the discharge capacity of the reference cell, which is 16.16  $\text{A m}^{-2}$ . The decreased size of the confidence interval seems to be related to the interaction

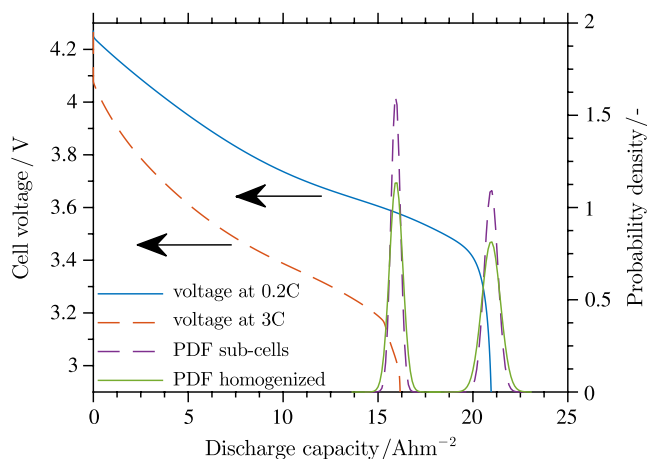


**Figure 10.** Discharge curves at 0.2 and 3 C of the reference cell simulated with the extended model. PDFs of the discharge capacity at 2.9 V of the extended model considering sub-cells and of the model with homogenized membrane properties. Standard deviations are  $\pm 5\%$  for all uncertain parameters.

between different sub-cells and balancing of differences in performance as shown below.

To illustrate the influence of sub-cell variations and the interaction between sub-cells, **Figure 11** shows exemplary current distribution between sub-cells at one PEM sample point at 3 C. In the applied parameter set, the anode layer thickness and the porosity of the corresponding cathode of one sub-cell (sub-cell 4) are increased to 71.51  $\mu\text{m}$  and 36.01%, respectively, whereas the overall loading is constant in all sub-cells. The other four sub-cells have the parameters of the reference cell. During the first 0.2 h of operation, all sub-cells have a similar current density. When the slope of the discharge curve becomes more negative toward the end of operation, there are significant and rapid changes in the current distribution between the different sub-cells on a small time scale of tens of seconds. The current density in sub-cell 4 increases slightly before it drops significantly after about 0.22 h. The other four areas together balance this drop by an increase in their current density. Eventually after about 0.23 h, the current in sub-cell 4 drops by about 20%, which is more than the remaining areas that can balance on a suitable voltage level, thus causing a large voltage drop that reaches the lower cutoff voltage.

The observed dynamics in the current distribution is related to the slightly differing surface concentrations of lithium in the active material of different sub-cells. As the surface concentration in the active material in, for example, the anode of a sub-cell decreases, its potential losses increase and the cell voltage decreases. To ensure equality of voltage between such a sub-cell and the other sub-cells, the current of this sub-cell decreases. In the battery depicted in Figure 11, the effective ionic resistance of sub-cell 4 is reduced and the active surface and the layer thickness are increased. The latter leads to a higher current density in the first seconds and a lower current in the next about 0.2 h. The increased layer thickness leads to areas in sub-cell 4 that are less utilized within the first 0.2 h. These areas are utilized when the current density of sub-cell 4 increases above the current density in the other sub-cells.

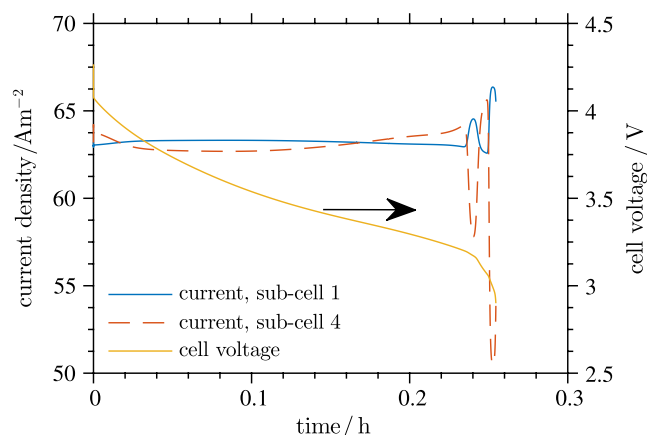


**Figure 11.** Current distribution between sub-cells with different electrode properties. Sub-cell 1 is identical to the sub-cells 2, 3, and 5. In sub-cell 4, the anode layer thickness is increased to 71.51  $\mu\text{m}$  and the cathode porosity to 36.01%. Apart from these changes, standard parameters are used.

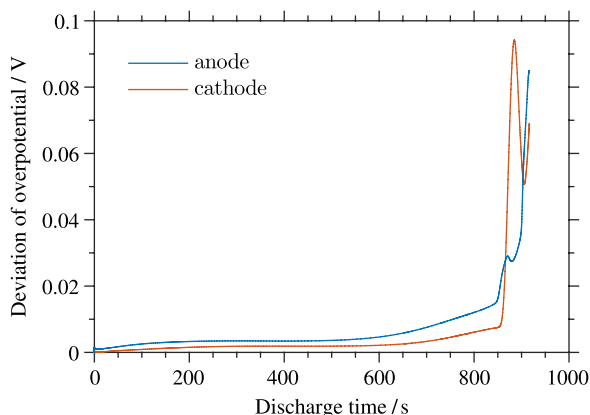


**Figure 12.** Maximum deviation of the overpotential between sub-cells with different electrode properties.

Parallel to changes in current distribution, there is high fluctuation in the local overpotentials of up to 100 mV. For illustration, see **Figure 12**. The figure shows the maximum difference of the overpotential between the different sub-cells.

The detrimental influence of local high overpotentials regarding cell degradation is discussed in refs. [52,53]. In-depth discussion of this is beyond the scope of this work, but it shows that inhomogeneities in cell properties might be a cause for degradation. At low cell currents, a positive effect could also be achieved. The dynamic balancing could compensate poor performance of some sub-cells and allow a further utilization of the theoretical battery capacity due to the operation at a lower local current density compared with a homogenized cell.

While the results regarding the spatial current distribution cannot be validated experimentally in this work, they are highly reasonable. For instance, in experiments of Pastor-Fernández et al., similar current profiles were measured for a parallel set of 18 650 cells with different states of health.<sup>[54]</sup> In addition, similar effects of a nonuniform current distribution were observed in experiments with segmented fuel cells and spatially reduced active area.<sup>[55–57]</sup> Furthermore, overpotential overshooting due to nonsteady currents was seen in the simulations of a direct methanol fuel cell.<sup>[58]</sup> The findings are also in accordance with the simulation results of a battery pack model based on ECMs<sup>[47]</sup> and the explanation regarding the detrimental effects of local imbalances or pore blockage of the electrodes, leading to lithium plating and accelerated aging due to locally higher current densities<sup>[59,60]</sup> and resulting overpotentials.

In summary, our studies show that sub-cell level property deviations affect the discharge capacity due to nonuniform spatial current distribution. This effect alters the mean discharge capacity and the standard deviation of the cells. Hence, there is a need for additional quality requirements for small-scale variation in the production process, as their influence on local overpotentials is at least as important as the influence of cell-to-cell deviations. For instance, for the investigated stacked pouch cells, the use of sheets of different batches should be avoided and a continuous process should be implemented.

## 5. Summary and Conclusions

A model-based approach for the UQ of LIB product parameters is introduced that is feasible to evaluate cell-to-cell deviations and sub-cell level deviations by applying an extended Doyle–Newman model. A nested PEM is applied for a large number of independent normal distributed parameters, which provides a global SA that shows a change in the sensitivity of the investigated parameters depending on the applied C-rate. The method is assessed by comparing with a first-order global SA by parameter variation and an MC approach. The PEM is highly efficient regarding computational costs but is limited in terms of imaging minor sensitivities. In addition, at low C-rates, the PEM fails due to the nondifferentiability of the system.

The global first-order SA shows a significant linearity at low C-rates and nonlinearity of the investigated electrochemical system at high C-rates. The presence of four types of sensitivities is observed, which have to be taken into account differently in processes such as UQ or optimization. Application of the introduced UQ approach in large-scale cell production showed that there is a need to control certain parameters within tighter constraints than others. In general, important parameters are those affecting the theoretical capacity such as layer thickness of the limiting electrode. In addition, the discharge voltage is sensitive to the parameters of the electrode that bears the steeper half-cell potential curve. In the investigated case, this was the cathode despite the anode causing the limitation of the discharge capacity. For the investigated cell, key parameters for performance are the cathode's specific capacity ( $\Delta c_{\max,c}$ ) and the cathode layer thickness ( $\delta_{e,c}$ ). Hence, the calendaring steps should be thoroughly monitored.

The investigation of the influence of sub-cell level deviations showed that the effect of small-scale deviations is less important for the performance of a cell at low C-rates, but it may cause locally higher overpotentials that can be detrimental regarding the long-term performance of the cell, especially at high C-rates. This leads to higher quality requirements for small-scale process deviations within a cell.

In conclusion, the results of this work show that a model-based approach is feasible to investigate and optimize the non-ideal LIB manufacturing process to reduce costs and time efforts of the development of, for example, next-generation batteries. In addition, the conducted global SA and the novel model approach showed electrochemical processes and interactions between product properties and cell performance.

## Acknowledgments

This work was supported by the German Federal Ministry for Economic and Affairs of Energy through funding the project “Data-Mining in der Produktion von Lithium-Ionen Batteriezellen (DaLion)” (03ET6089). The authors gratefully thank Ruben Leithoff of the Institute of Machine Tools and Production Technology (IWF) and Tobias Jansen of the Institute of Joining and Welding (IFS) for the cell assembly in the Battery LabFactory Braunschweig (BLB) and Kerstin Ryll of the Institute for High Voltage Technology and Electrical Power Systems (elenia) and the Institute of Environmental and Sustainable Chemistry (IÖNC) for conducting the electrochemical cell characterization. The efforts of Wolfgang Haselrieder in the management of the cell production in the BLB are also gratefully acknowledged. X. Xie acknowledges the support from the

International Max Planck Research School for Advanced Methods in Process and Systems Engineering, MPI Magdeburg.

## Conflict of Interest

The authors declare no conflict of interest.

## Keywords

Li-ion batteries, modeling, production process, uncertainty quantification methods

Received: February 15, 2019

Revised: March 22, 2019

Published online:

- 
- [1] M. Westermeier, G. Reinhart, T. Zeilinger, in 3rd Int. Electr. Drives Prod. Conf., IEEE, Nuremberg **2013**.
- [2] Y.-B. Yi, C.-W. Wang, A. M. Sastry, *J. Eng. Mater. Technol.* **2006**, 128, 73.
- [3] C.-W. Wang, Y.-B. Yi, A. M. Sastry, J. Shim, K. A. Striebel, *J. Electrochem. Soc.* **2004**, 151, A1489.
- [4] W. Haselrieder, S. Ivanov, D. K. Christen, H. Bockholt, A. Kwade, *ECS Trans.* **2013**, 50, 59.
- [5] A. van Bommel, R. Divigalpitiya, *J. Electrochem. Soc.* **2012**, 159, A1791.
- [6] G. F. Yang, S. K. Joo, *Electrochim. Acta* **2015**, 170, 263.
- [7] H. Zheng, L. Tan, G. Liu, X. Song, V. S. Battaglia, *J. Power Sources* **2012**, 208, 52.
- [8] G. Lenze, F. Röder, H. Bockholt, W. Haselrieder, A. Kwade, U. Krewer, *J. Electrochem. Soc.* **2017**, 164, 1223.
- [9] J. R. Dahn, T. Zheng, Y. Liu, J. S. Xue, *Mater. Sci.* **1995**, 270, 590.
- [10] C. Edouard, M. Petit, C. Forgez, J. Bernard, R. Revel, *J. Power Sources* **2016**, 325, 482.
- [11] M. Hadigol, K. Maute, A. Doostan, *J. Power Sources* **2015**, 300, 507.
- [12] B. Kenney, K. Darcovich, D. D. MacNeil, I. J. Davidson, *J. Power Sources* **2012**, 213, 391.
- [13] S. Santhanagopalan, R. E. White, *Int. J. Electrochem.* **2012**, 2012, 1.
- [14] U. Krewer, F. Röder, E. Harinath, R. D. Braatz, B. Bedürftig, R. Findeisen, *J. Electrochem. Soc.* **2018**, 165, A3656, ISSN 0013-4651, DOI: 10.1149/2.1061814jes.
- [15] S. Santhanagopalan, R. E. White, *ECS Trans.* **2007**, 3, 243.
- [16] S. Santhanagopalan, R. E. White, *Electrochem* **2012**, 2012, 1.
- [17] J. Vazquez-Arenas, L. E. Gimenez, M. Fowler, T. Han, S. K. Chen, *Energy Convers. Manag.* **2014**, 87, 472.
- [18] V. Ramadesigan, K. Chen, N. A. Burns, V. Boovaragavan, R. D. Braatz, V. R. Subramanian, *J. Electrochem. Soc.* **2011**, 158, A1048.
- [19] A. P. Schmidt, M. Bitzer, A. W. Imre, L. Guzzella, *J. Power Sources* **2010**, 195, 5071.
- [20] N. Lin, X. Xie, R. Schenkendorf, U. Krewer, *J. Electrochem. Soc.* **2018**, 165, A1169.
- [21] S. F. Schuster, M. J. Brand, P. Berg, M. Gleissenberger, A. Jossen, *J. Power Sources* **2015**, 297, 242.
- [22] M. Dubarry, C. Truchot, M. Cugnet, B. Y. Liaw, K. Gering, S. Sazhin, D. Jamison, C. Michelbacher, *J. Power Sources* **2011**, 196, 10328.
- [23] F. Röder, S. Sonntag, D. Schröder, U. Krewer, *Energy Technol.* **2016**, 4, 1588.
- [24] D.-W. Chung, P. R. Shearing, N. P. Brandon, S. J. Harris, R. E. Garcia, *J. Electrochem. Soc.* **2014**, 161, A422.
- [25] M. Farkhondeh, C. Delacourt, *J. Electrochem. Soc.* **2012**, 159, A177.
- [26] H. Dreger, H. Bockholt, W. Haselrieder, A. Kwade, *J. Electron. Mater.* **2015**, 44, 4434.
- [27] H. Bockholt, W. Haselrieder, A. Kwade, *ECS Trans.* **2013**, 50, 25.
- [28] H. Bockholt, M. Indrikova, A. Netz, F. Golks, A. Kwade, *J. Power Sources* **2016**, 325, 140.
- [29] B. Westphal, H. Bockholt, T. Gunther, W. Haselrieder, A. Kwade, *ECS Trans.* **2015**, 64, 57.
- [30] V. Ramadesigan, P. W. C. Northrop, S. De, S. Santhanagopalan, R. D. Braatz, V. R. Subramanian, *J. Electrochem. Soc.* **2012**, 159, R31, ISSN 0013-4651, DOI: 10.1149/2.018203jes.
- [31] S. Mendoza, M. Rothenberger, J. Liu, H. K. Fathy, *IFAC-PapersOnLine* **2017**, 50, 7314.
- [32] D. C. López, G. Wozny, A. Flores-Tlacuahuac, R. Vasquez-Medrano, V. M. Zavala, *Ind. Eng. Chem. Res.* **2016**, 55, 3026.
- [33] G. W. Tyler, *Can. J. Math.* **1953**, 5, 393.
- [34] E. Rosenblueth, *Proc. Natl. Acad. Sci. U. S. A.* **1975**, 72, 3812.
- [35] Z. Lin, W. Li, *Reliab. Eng. Syst. Saf.* **2013**, 111, 106.
- [36] R. Schenkendorf, in Proc. 2nd Eur. Conf. Progn. Heal. Manag. Soc., Fort Worth, **2014**.
- [37] R. C. Smith, *Uncertainty Quantification: Theory, Implementation, and Application*. Society for Industrial and Applied Mathematics, Philadelphia **2014**.
- [38] J. Marcicki, M. Canova, A. T. Conlisk, G. Rizzoni, *J. Power Sources* **2013**, 237, 310.
- [39] A. M. Colclasure, R. J. Kee, *Electrochim. Acta* **2010**, 55, 8960.
- [40] M. Doyle, T. F. Fuller, J. Newman, *J. Electrochem. Soc.* **1993**, 140, 1526.
- [41] N. Legrand, S. Raël, B. Knosp, M. Hinaje, P. Desprez, F. Lapique, *J. Power Sources* **2014**, 251, 370.
- [42] Z. Liu, P. P. Mukherjee, *J. Electrochem. Soc.* **2014**, 161, E3248.
- [43] B. Westphal, H. Bockholt, T. Günther, W. Haselrieder, A. Kwade, *ECS Trans.* **2015**, 64, 57.
- [44] W. M. Haynes, *CRC Handbook of Chemistry and Physics*, CRC Press, Boca Raton, FL, 91 edn. **2011**.
- [45] M. Ecker, S. Kabitz, I. Laresgoiti, D. U. Sauer, *J. Electrochem. Soc.* **2015**, 162, A1849.
- [46] M. S. Whittingham, *Chem. Rev.* **2004**, 104, 4271.
- [47] M. Dubarry, N. Vuillaume, B. Y. Liaw, *J. Power Sources* **2009**, 186, 500.
- [48] M. Dubarry, A. Devie, B. Y. Liaw, *J. Power Sources* **2016**, 321, 36.
- [49] K. Smith, C.-Y. Wang, *J. Power Sources* **2006**, 160, 662.
- [50] L. Hoffmann, J.-K. Grathwol, W. Haselrieder, R. Leithoff, T. Jansen, K. Dilger, K. Dröder, A. Kwade, M. Kurrat, *Energy Technol.* **2019**, 7, 1900196.
- [51] T. P. Heins, N. Schlüter, U. Schröder, *ChemElectroChem* **2017**, 4, 1.
- [52] N. Legrand, S. Raël, B. Knosp, M. Hinaje, P. Desprez, F. Lapique, *J. Power Sources* **2014**, 251, 370.
- [53] C. von Lüders, V. Zinth, S. V. Erhard, P. J. Osswald, M. Hofmann, R. Gilles, A. Jossen, *J. Power Sources* **2017**, 342, 17.
- [54] C. Pastor-Fernández, T. Bruen, W. D. Widanage, M. A. Gama-Valdez, J. Marco, *J. Power Sources* **2016**, 329, 574.
- [55] T. V. Reshetyenko, K. Bethune, R. Rocheleau, *J. Power Sources* **2012**, 218, 412.
- [56] T. V. Reshetyenko, K. Bethune, M. A. Rubio, R. Rocheleau, *J. Power Sources* **2014**, 269, 344.
- [57] T. V. Reshetyenko, J. St-Pierre, *J. Power Sources* **2016**, 333, 237.
- [58] U. Krewer, A. Kamat, K. Sundmacher, *J. Electroanal. Chem.* **2007**, 609, 105.
- [59] S. S. Zhang, *J. Power Sources* **2006**, 161, 1385.
- [60] L. Somerville, J. Baren, S. Trask, P. Jennings, A. McGordon, C. Lyness, I. Bloom, *J. Power Sources* **2016**, 335, 189.